

Experimental investigation of the effect of nickel on the electrical resistivity of Fe-Ni and Fe-Ni-S alloys under pressure

ANNE POMMIER^{1,*}

¹UC San Diego–SIO–IGPP, 8800 Biological Grade, La Jolla, California 92093-0225, U.S.A.

ABSTRACT

Electrical resistivity experiments were conducted on three alloys in the iron-rich side of the Fe-Ni(-S) system (Fe-5 wt% Ni, Fe-10 wt% Ni, Fe-10 wt% Ni-5 wt% S) at 4.5 and 8 GPa and up to 1900 K using the multi-anvil apparatus and the 4-electrode technique. For all samples, increasing temperature increases resistivity. At a specified temperature, Fe-Ni(-S) alloys are more resistive than Fe by a factor of about 3. Fe-Ni alloys containing 5 and 10 wt% Ni present comparable electrical resistivity values. The resistivity of Fe-Ni(-S) alloys is comparable to the one of Fe = 5 wt% S at 4.5 GPa and is about three times higher than the resistivity of Fe = 5 wt% S at 8 GPa, due to a different pressure dependence of electrical resistivity between Fe-Ni and Fe-S alloys. Based on these electrical results and experimentally determined thermal conductivity values from the literature, lower and upper bounds of thermal conductivity were calculated. For all Ni-bearing alloys, thermal conductivity estimates range between ~12 and 20 W/(m·K) over the considered pressure and temperature ranges. Adiabatic heat fluxes were computed for both Ganymede's core and the Lunar core, and heat flux values suggest a significant dependence to both core composition and the adiabatic temperature. Comparison with previous thermochemical models of the cores of Ganymede and the Moon suggests that some studies may have overestimated the thermal conductivity and hence, the heat flux along the adiabat in these planetary cores.

Keywords: Iron-nickel alloys, metallic cores, electrical resistivity, multi-anvil apparatus, Ganymede, the Moon

INTRODUCTION

The metallic cores of terrestrial planets and moons are composed of iron-nickel alloy that contains different amounts of light elements (such as S, Si, and C). Several weight percentages of nickel are thought to be present in these planetary cores, based on mass balance calculations and on iron-rich meteorites geochemistry (e.g., McDonough and Sun 1995; Jarosewich 1990). For instance, geochemical models have suggested that about 5.5 wt% Ni is present in the Earth's core (e.g., McDonough and Sun 1995), and an estimate of about 9 wt% Ni in the Lunar core has been suggested by Righter et al. (2017), assuming a bulk Moon Ni content of 2200 ppm, a core fraction of 2 mass% and using calculations of the metal–silicate partition coefficient of Ni. Meteorite geochemistry has indicated that the Martian core also likely contains several weight percentages Ni, with Fe, Ni, and S, possibly representing the major components of the planet's core (e.g., Wänke and Dreibus 1988; Lodders and Fegley 1997).

Several investigations have been conducted to understand the effect of nickel on the chemical and physical properties of iron alloys, and therefore to determine the influence of Ni on the structure and dynamics of metallic cores. The effect of nickel on the phase diagram of iron is detectable but small (e.g., Lin et al. 2002), and in particular, Ni stabilizes the face-centered cubic (fcc) structure under high pressure and temperature (e.g., Côté et al.

2012). It was proposed that Ni does not affect significantly the melting curve of the Fe-rich side of the Fe-S system at the core conditions in small terrestrial bodies (less than 100 K of difference between Fe-S and (Fe,Ni)-S, Stewart et al. 2007), though it might be more significant at high pressure relevant to the Earth's core (Komabayashi et al. 2019). This suggests that nickel, contrary to light-alloying components such as sulfur, is unlikely to affect the onset of core crystallization of small planets and moons. Nickel may have affected the partitioning behavior of heavy iron isotopes during core formation (Elardo and Shahar 2017), but no measurable effect of nickel concentration on the partitioning of siderophile elements has been observed under Earth's core conditions (Ni, Cr, V; Huang and Badro 2017). Experimental studies of Fe-Ni alloys under pressure have demonstrated that Ni has a very small effect on several material properties, such as density, sound velocity, and compressibility (e.g., Mao et al. 1990; Lin et al. 2003; Kantor et al. 2007; Martorell et al. 2013, 2015; Kawaguchi et al. 2017; Wakamatsu et al. 2018; Morrison et al. 2019), justifying the use of Ni-free iron alloys as core analogues in mineral physics experiments.

The investigation of core dynamics requires constraining the superadiabatic heat flux, i.e., the heat that is available to drive convection, which depends strongly on the thermal resistivity of the core materials. Measurements of the thermal resistivity of Fe-Ni alloys under high temperature are scarce, but at atmospheric pressure and high temperature (>1673 K), experiments have suggested that Ni does not affect significantly the thermal resistivity

* E-mail: pommier@ucsd.edu. Orcid 0000-0003-3182-1912.

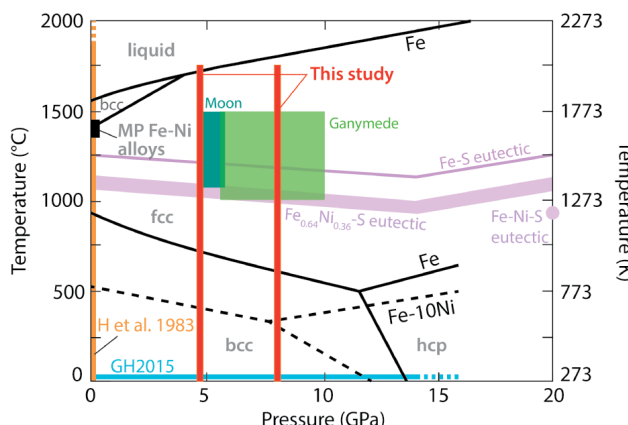


FIGURE 1. Phase relationships in Fe, Fe-Ni, and Fe-Ni-S systems and summary of experimental conditions in previous electrical works on Fe-Ni alloys and in this study. Phase diagrams for solid phases are from Huang et al. (1988). Fe-Ni alloys melting point (MP) temperature at 1 atm from Hansen (1958) and Fe melting curve from Ma et al. (2004) and Anzellini et al. (2013). Fe-S and Fe-Ni-S eutectic curves are from Fei et al. (2000); Li et al. (2001); Stewart et al. (2007); Zhang and Fei (2008); Morard et al. (2007). Fe-Ni-S eutectic melting temperature at 20 GPa comes from Zhang and Fei (2008) for a Ni/(Ni+Fe) ratio of 0.09. GH2015 = Gomi and Hirose 2015; H et al. 1983 = Ho et al. (1983). Comparison with the expected pressure and temperature conditions for the core of the Earth's moon and Ganymede are also shown (green rectangles) (after Breuer et al. 2015). (Color online.)

of Fe-Ni melts (Watanabe et al. 2019). Lower bound estimates of thermal resistivity of Fe-Ni alloys can also be obtained from electrical resistivity measurements (Watanabe et al. 2019). The electrical resistivity of Fe-Ni alloys has been well documented at atmospheric pressure, with the effect of temperature and composition being investigated systematically (e.g., Ho et al. 1983 and references therein; Kita and Morita 1984). At a specified temperature, resistivity increases with the nickel content, and at high temperature, the electrical resistivity of molten alloys presents a linear temperature dependence. The effect of nickel content on iron resistivity was found to be significant both in the solid and the liquid state in these studies and to be higher at low temperature than at high temperature. Electrical resistivity is also a subtle probe of the Invar region, of the martensitic and austenitic metastable states, and of the magnetic transition across the Curie temperature in Fe-Ni alloys (e.g., Ho et al. 1983 and references therein). Under high pressure (up to 70 GPa) and at room temperature, electrical resistivity measurements in the iron-rich portion of the Fe-Ni system (up to 15 wt% Ni) have highlighted a non-negligible effect of Ni on the electrical properties of iron alloys, with nickel increasing the alloy resistivity (Gomi and Hirose 2015). With increasing pressure, an increase in resistivity by a factor of ~2 followed by a drop in resistivity upon the body-centered cubic (bcc) to hexagonal-close-packed (hcp) structure transition was observed, which was also reported by Kuznetsov et al. (2007) at 425 K and ~8 GPa. Based on the extrapolation of their data at room temperature to high temperatures, Gomi and Hirose (2015) suggested that the effect of Ni on resistivity might become negligible under Earth's core conditions, due to resistivity "saturation" (Gomi et al. 2013; Pozzo and Alfè 2016;

Wagle et al. 2019). This saturation depends on the mean free path of the electrons, which directly depends on temperature (thermal saturation) and can be enhanced by the presence of impurities (chemical saturation).

These previous thermal and electrical resistivity studies of Fe-Ni alloys have been conducted at pressure and temperature conditions different from the ones of the cores in small planets and moons (Fig. 1), raising the question of the effect of nickel on the core cooling processes of Mars-sized or smaller bodies. Here the effect of Ni (up to 10 wt%) on the electrical resistivity of Fe-Ni(±)S samples has been investigated experimentally up to 8 GPa and ~1900 K. Based on the electrical resistivity results, thermal conductivity is calculated and used to compute adiabatic heat fluxes in the cores of Ganymede and the Moon.

ELECTRICAL EXPERIMENTS AND ANALYSES

Electrical experiments were performed on three compositions: Fe-5 wt% Ni, Fe-10 wt% Ni, and Fe-5 wt% Ni-3 wt% S (referred to as Fe-5Ni, Fe-10Ni, and Fe-10Ni-5S, respectively). Electrical results for Fe and Fe-5 wt% S from Pommier (2018) were added to the data set for comparison. The detailed compositions are listed in Table 1. The starting materials were homogeneous powder mixtures of high-purity (>99%) Fe, Ni, and FeS powders (Alfa Aesar) and stored either in a sealed container placed in a desiccator or in a vacuum oven at 110 °C until use.

Electrical experiments were conducted at 4.5 and 8 GPa in the multi-anvil apparatus at the Planetary and Experimental Petrology Laboratory at UCSD-SIO, using tungsten carbide cubes with a corner-truncation edge length of 8 mm and MgO octahedral pressure media with an edge length of 14 mm. The COMPRES electrical cell used as part of the experiments consists of a sample sleeve (MgO) that contains three alumina rings isolated by metal disks made of high-purity iron (Pommier et al. 2019). As illustrated in Figure 2, the sample is placed in the middle ring (ID of 1.45 mm, thickness of 1.25 mm). A rhenium heater was used and two 4-bore MgO beads each contain two W-Re wires. The temperature was monitored by a Type-C (W_9Re_5 - W_7Re_{26}) thermocouple. The cell contains two thermocouples that are in contact with the Fe metal disks, the four wires serving as electrodes. All MgO parts were fired at >1000 °C and stored in a desiccator.

Electrical experiments were performed under quasi-hydrostatic conditions in the multi-anvil press during cooling and heating cycles using the four-electrode method (e.g., Pommier 2018) (Table 2). A dwell was first applied to the sample at a temperature below the eutectic temperature (~600 °C). All experiments were quenched at the highest temperature by shutting off the power to the heating system. The electrode system consists of two wires for voltage drop measurement and two wires for current measurement. A current with a controlled voltage (DC potential of 1 V and AC amplitude between 500 and 1000 mV) was imposed during the measurement. The bulk electrical resistance was measured using an impedance meter (1260 Solartron Impedance/Gain-Phase Analyzer). A manual shift was used to either read temperature or the electrical response. The measured electrical resistance R and sample geometric factor G are used to calculate the electrical resistivity ρ

$$\rho = R \times G \text{ with } G = A/l \quad (1)$$

with A is the area of one electrode (metal disk with a diameter of 2.5 mm), and l is the thickness of the sample (determined using SEM images of the recovered sample). Relative errors on values of ρ were calculated on the basis of errors on A and l as well as propagated errors on each measured value of resistance R (Table 2). The sample resistance was obtained from the measured (bulk) resistance value by removing the contribution from the iron disks and the alumina ring (Pommier et al. 2019).

Longitudinal sections of the experimental charges were mounted and polished for analytical and chemical characterization using scanning electron microscope (SEM)

TABLE 1. Composition of starting materials

System	wt% Ni	mol% Ni	wt% S	mol% S
Fe ^a	—	—	—	—
Fe-5S ^a	—	—	5.0	8.40
Fe-5Ni	5.0	4.77	—	—
Fe-10Ni	10.0	9.56	—	—
Fe-10Ni-5S	10.0	8.40	5.0	7.69

^a From Pommier (2018).

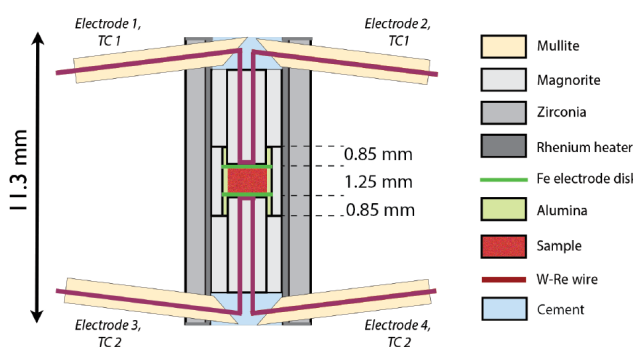


FIGURE 2. COMPRES electrical cell developed for the 4-electrode experiments using 14/8 assemblies. Thermocouple wires are also used as electrodes and are in contact with Fe disks. (Color online.)

imaging and an electron probe microanalyzer (EPMA) at the University of Lille, France. Backscattered electron images and quantitative chemical analyses of Fe-Ni-S samples were obtained with a Cameca SX 100 electron microprobe using wavelength dispersive spectrometry (WDS). Analyses were performed with a 15 kV accelerating voltage and a beam current of 40 nA. The phases were analyzed with a focused beam. Natural and synthetic standards were used to quantify the amount of different elements (Fe_2O_3 for Fe and O, Ni metal for Ni, ZnS for S, or those for Al and W metal for W).

RESULTS

Chemical and textural analyses

Chemical analyses of retrieved samples using the electron microprobe and EDS-SEM techniques are presented in Table 3 and Figure 3. No significant contamination of the samples by the

TABLE 2. Summary of electrical experiments

Composition	Pressure (GPa)	Temperature (K)	Initial dwell duration (h)	Uncertainty on resistivity (%) ^b
Fe ^a	4.5	720–1973	–	3.7–4.9
Fe-5S ^a	4.5	628–1891	3.5	1.8–2.5
Fe-5S ^a	8.0	471–1506	2	4.7–9.9
Fe-5Ni	4.5	724–1894	2	4.5–5.1
Fe-5Ni	4.5	771–1722	1	4.5–4.8
Fe-5Ni	8.0	921–1874	2	6.6–6.9
Fe-10Ni	4.5	867–1904	2.5	3.4–3.9
Fe-10Ni	4.5	676–1771	1	4.9–5.8
Fe-10Ni	8.0	1045–1769	2.5	8.1–8.4
Fe-10Ni-5S	4.5	868–1844	1.5	3.5–3.8
Fe-10Ni-5S	8.0	898–1903	2.5	3.9–4.2

^a From Pommier (2018).

^b $\Delta\rho = |\Pi^2/\| \times \Delta R + |2\Pi Rr/\| \times \Delta r + |-\Pi Rr^2/\|^2 \times \Delta l$ with ρ the resistivity, l the sample thickness, R the electrical resistance of the sample, and r the radius of the electrode disk.

alumina or the magnesia rings is observed. A few isolated FeO grains are observed in some samples, but no significant amount of oxygen is measured using electron microprobe analyses (Table 3, Fig. 3). Some samples present a small amount of W in the dendritic phase, which is consistent with unavoidable interactions with the thermocouple wires at high temperature. No strong compositional heterogeneity is observed across the recovered samples; an EPMA profile performed in the Fe-10Ni sample at 8 GPa illustrates this compositional homogeneity (Fig. 3).

SEM images of recovered samples are available in Supplemental¹ Figure S1. The retrieved samples present textures of fully molten alloys following rapid solidification. The electrical cell geometry was well-preserved during the experiment, minimizing uncertainty in the geometric factor calculations. Although dendritic patterns are visible in all samples, the texture of quenched Fe-Ni-S samples presents a higher contrast between dendritic structures (light color) and the surrounding phase (dark color) than the Fe-Ni samples. This can be explained by the presence of S in the quenched phase surrounding the dendrites, that increases the contrast between the two phases (the dark region is a S-rich quenched melt, due to a lower Fe content).

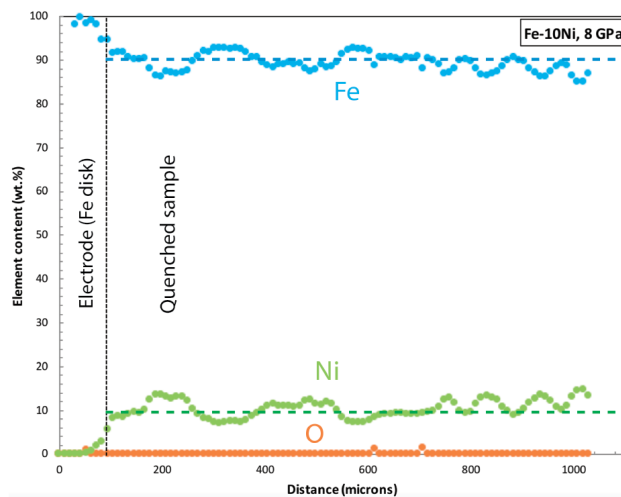


FIGURE 3. EPMA profile in recovered sample (Fe-10Ni, at 8 GPa) showing the concentration of iron (blue), nickel (green), and oxygen (orange) from the Fe electrode disk to most of the sample's thickness. The variations in the iron and nickel contents are consistent with crossing the quenched phases. The average values of Fe and Ni contents show a homogenous composition (90 wt% Fe, 10 wt% Ni) in the retrieved molten sample. (Color online.)

TABLE 3. Chemical analyses on recovered samples (in wt% norm. to 100; bdl = below detection limit)

Starting material	Quenched T (K)	P (GPa)	Phase ^a	Fe	Ni	S	W	O	Al
Electron microprobe spot analyses									
Fe-10Ni-5S	1844	4.5	"Oak leaf" phase (5) Joints (3)	93.88 64.31	4.567 2.281	0.076 31.88	1.276 0.078	0.326 bdl	bdl bdl
Fe-10Ni-5S	1903	8.0	"Oak leaf" phase (5) Joints (3)	90.25 66.49	4.163 2.816	0.093 28.60	4.604 0.898	bdl bdl	bdl bdl
EDS-SEM analyses									
Fe-5Ni	1894	4.5	Bulk sample	95.35	4.654	–	–	–	–
Fe-10Ni	1904	4.5	Bulk sample	93.64	6.360	–	–	–	–
Fe-10Ni	1769	8.0	Bulk sample Electrode disk	92.88 99.54	7.118 0.460	–	–	–	–

^a Numbers in parentheses correspond to the number of analyses.

Electrical resistivity results

The electrical resistivity results as a function of temperature are presented in Figures 4 and 5 and the electrical resistivity as a function of the amount of alloying agent(s) is illustrated in Figure 6. Reproducibility of the electrical measurements was checked by repeating two experiments on Fe-5Ni and Fe-10Ni samples at 4.5 GPa (Table 2). The dependence of resistivity to temperature is comparable for all samples: at 4.5 GPa and at temperature higher than the α - γ (or bcc-fcc) transition, the electrical resistivity increases by a factor of about 1.6–1.7 for pure iron, and of about 1.3–1.4 for Fe-5Ni, Fe-10Ni, and Fe-Ni-S. This increase in resistivity with temperature is linear at high temperature for the Fe-Ni samples. The bcc-fcc transition in the solid state is clearly identified (especially at 4.5 GPa), marked by a change in slope around 900 K. The onset of melting, which is characterized by a small increase in resistivity for Fe and Fe-5S, is not clearly identified for Ni-bearing samples, both at 4.5 and 8 GPa (Figs. 4 and 5).

The experimental results suggest that the presence of Ni increases the resistivity of both S-free and S-bearing alloys; at a specified pressure and temperature, Fe-Ni alloys are more resistive than pure iron and the Fe-Ni-S alloy is more resistive than Fe-S (Figs. 4 and 5). In particular, the addition of 5 wt% Ni to molten iron increases electrical resistivity by a factor of 4, both at 4.5 and 8 GPa (Fig. 6; at 8 GPa, the resistivity of pure iron is from Deng et al. 2013 and Silber et al. 2018). However, the difference in resistivity between Fe-5Ni and Fe-10Ni is negligible, as the Fe-10Ni samples present a similar or, at high temperature, a slightly higher resistivity than the Fe-5Ni samples (Figs. 5 and 6). At 4.5 GPa and over 900–1700 K, a difference in resistivity of a factor of about 3 is observed between pure iron and Fe-Ni samples and may increase slightly at pressure >4.5 GPa. The Fe-Ni-S sample is slightly more resistive than the Fe-Ni samples at 4.5 GPa, but no significant difference is observed between the resistivity of the Fe-Ni samples and that of Fe-Ni-S at 8 GPa.

At 4.5 GPa and over the investigated temperature range, the nickel impurity resistivity is significant and comparable to the effect of sulfur: the resistivity of an iron alloy containing 5 wt% or 10 wt% Ni (4.77 and 9.56 mol% Ni, respectively) is comparable to the resistivity of an iron alloy containing 5 wt% S (8.4 mol% S) (Figs. 5 and 6). At 8 GPa, the difference in resistivity between Ni-bearing and Ni-free alloys is higher than at 4.5 GPa, with Ni-bearing samples being significantly more resistive than Fe and Fe-5S (Figs. 5 and 6).

The pressure effect is negligible for the investigated Fe-Ni samples, which contrasts with the Fe-S system. For instance, at 1300 K and between 4.5 and 8 GPa, electrical resistivity decreases by a factor of 1.8 for pure Fe and of 2.9 for Fe-5S (8.4 mol% S) (and this factor increases for higher S contents up to 50 mol% S, Pommier 2018), whereas this factor is only of 1.03 and 1.06 for Fe-5Ni (4.77 mol% Ni) and Fe-10Ni (9.56 mol% Ni), respectively (Fig. 4). For the Fe-Ni-S composition, this factor increases to a value of 1.13, which may suggest that the presence of sulfur increases the pressure dependence of iron alloys resistivity. As discussed below, the difference in pressure dependence of the resistivity between S-bearing and Ni-bearing alloys might be explained by the combination of at least two different factors: the alloy compressibility and the phase assemblage of the starting materials.

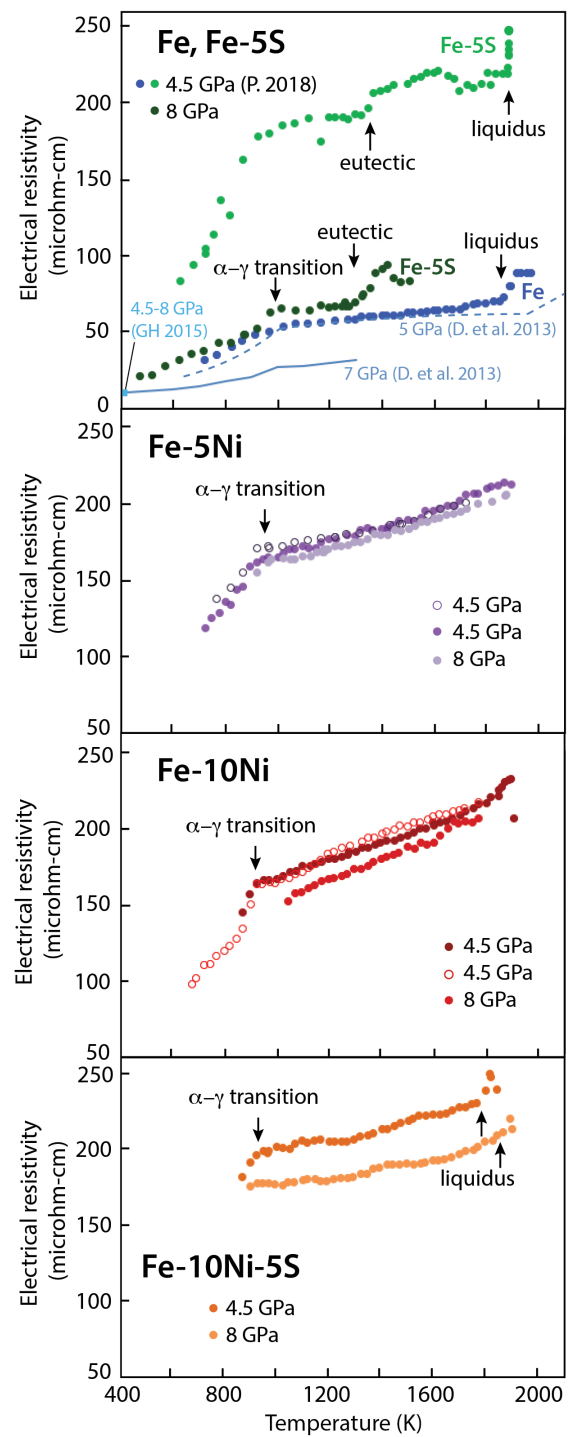


FIGURE 4. Electrical resistivity results as a function of temperature for the different compositions. (a) Resistivity of Fe and Fe-5S samples at 4.5 and 8 GPa, and comparison with previous works on pure iron at 7, 5, and 4.5–8 GPa. [D. et al. 2013 = Deng et al. (2013), GH2015 = Gomi and Hirose (2015), P. et al. 2018 = Pommier (2018)]. (b) Resistivity of Fe-5Ni samples at 4.5 and 8 GPa. The experiment at 4.5 GPa was repeated to check reproducibility. (c) Resistivity of Fe-10Ni samples at 4.5 and 8 GPa. The experiment at 4.5 GPa was also repeated to check reproducibility. (d) Resistivity of Fe-10Ni-5S samples at 4.5 and 8 GPa. The α - γ transition and the onset of melting are indicated with arrows on all plots. (Color online.)

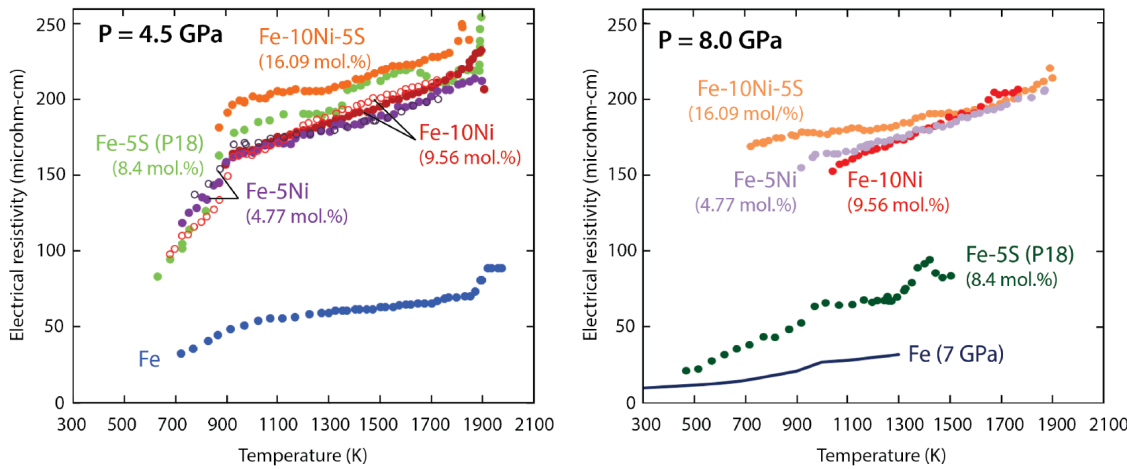


FIGURE 5. Electrical resistivity results at 4.5 GPa (left) and 8 GPa (right). A slight decrease in resistivity as pressure is increased is observed for Fe-Ni(-S) samples, whereas the pressure effect on resistivity is higher for Fe and Fe-S samples. Iron alloys are more resistive than pure iron and Fe-Ni(-S) samples are more resistive than Fe-5S at 8 GPa. Data at 7 GPa for pure Fe from Deng et al. (2013). (Color online.)

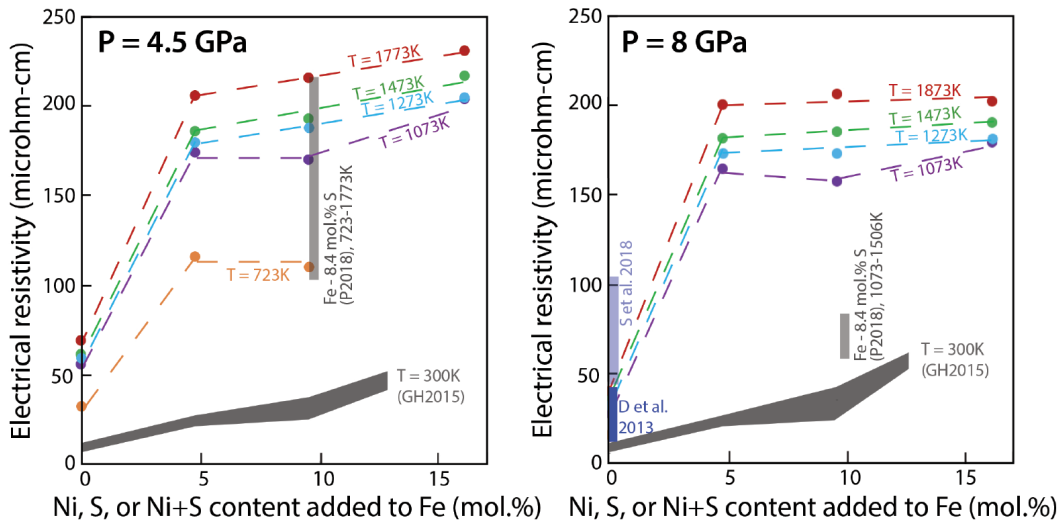


FIGURE 6. Effect of alloy chemistry on resistivity. Left side: data at 4.5 GPa. Right side: data at 8 GPa. A comparison with data on Fe-Ni at 300 K (Gomi and Hirose 2015), Fe-5S (Pommier 2018), and Fe (Deng et al. 2013; Silber et al. 2018) is provided. (Color online.)

IMPLICATIONS

Effect of nickel on electrical resistivity and comparison with previous works

Previous electrical experiments on Fe-Ni alloys under pressure (up to 70 GPa) have been conducted at 300 K by Gomi and Hirose (2015). As highlighted in Figure 6, their resistivity values at room temperature are lower than the ones measured in this study, which is consistent with the fact that temperature increases electrical resistivity. Over the 4.5–8 GPa pressure range, Gomi and Hirose (2015) measured a negligible effect of Ni content on the resistivity of Fe-Ni samples containing 5 and 10 wt% Ni at room temperature, and the present study suggests that this negligible effect persists under temperature (Figs. 4 and 5). At atmospheric pressure, electrical experiments also showed the increase in resistivity with increasing Ni content and/or temperature (Ho et al. 1983 and references therein). Resistivity values for molten Fe-Ni alloys containing up to 15 wt% Ni

at 1 atm are in broad agreement with the ones collected under pressure up to 8 GPa: in the molten state, electrical resistivity values are about 130–160 $\mu\Omega\cdot\text{cm}$ at 1 atm vs. ~ 150 – 200 $\mu\Omega\cdot\text{cm}$ at 4.5 and 8 GPa. However, at 300 K, a factor of up to 2.5 difference in resistivity is observed between different studies, as Ho et al. reported electrical resistivity values of 10–25 $\mu\Omega\cdot\text{cm}$ vs. ~ 8 – 10 $\mu\Omega\cdot\text{cm}$ from Gomi and Hirose (2015).

The present data set allows comparing the effect of Ni and S impurity on resistivity. As an alloying agent, the addition of sulfur increases the electrical resistivity of iron (Argyriades et al. 1959; Pommier 2018). At 4.5 GPa, the resistivity of Fe-Ni and Fe-S with a comparable amount of alloying component (9.56 mol% Ni and 8.4 mol% S; Table 1) is similar over the investigated temperature range (Fig. 5). At this pressure, the Fe-10Ni-5S sample, containing 16.09 mol% alloying agents (Table 1), presents only slightly higher resistivity values than the Fe-Ni and Fe-S samples, whereas at 8 GPa the difference in electrical resistivity corresponds to a factor of ~ 2.5 between

Fe-S and Fe-Ni-S samples and is negligible between Fe-Ni and Fe-Ni-S samples. This suggests that the effect of pressure on resistivity depends on the alloy chemistry, and in the Fe-10Ni-5S sample, the dependence of electrical resistivity to pressure is controlled by Ni impurity, not by S impurity. Different factors might explain these two observations; in particular, differences in compressibility and the phase assemblage could contribute to the contrasting pressure effect on resistivity. First, the Fe-S alloy is less dense than Fe and Ni-bearing iron alloys (e.g., Sanloup et al. 2000; Lin et al. 2004; Kawaguchi et al. 2017), and Fe-Ni alloys present a slightly higher density than pure Fe (e.g., Martorell et al. 2015; Watanabe et al. 2016). For instance, Fe-10S at 5 GPa and 1770 K has a density of about 5.65 g/cm³ (Sanloup et al. 2000) whereas the density of Fe-7.6Ni and Fe-7.6Ni-10S at a similar temperature and extrapolated to the same pressure is about 7.8 and 6.8 g/cm³, respectively (Kawaguchi et al. 2017). The Fe-S alloy is thus more compressible than pure Fe and Fe-Ni alloys, which can explain at least partly the higher pressure effect on the resistivity of Fe-5S than on one of the other investigated alloys. Second, in the Fe-Ni-S sample, the small pressure-dependence of resistivity suggests a control of the electrical properties by Ni rather than S, and this might be explained by the multi-phase assemblage of the starting materials. The Fe-Ni-S sample is likely a mixture of Fe-Ni(-S) alloy with a small volume fraction of Fe_{1-x}S, as the solubility of sulfur is low in solid fcc iron (e.g., Li et al. 2001; Hayashi et al. 2009). The low S solubility in fcc Fe could result in a minor role of sulfur in controlling the bulk resistivity, compared to the effect of nickel that substitutes for Fe. The presence of two phases in the solid Fe-Ni-S sample may account for why Fe-Ni-S and Fe-Ni resistivity present a similar *P* dependence. Further work is required to demonstrate whether or not these observations about the relative effect of nickel and sulfur on electrical resistivity also apply to pressures higher than 8 GPa.

Thermal conductivity estimates of Fe-Ni alloys

Watanabe et al. (2019) demonstrated that experimentally measured thermal conductivities of Fe-Ni melts at atmospheric pressure and high temperature (1700–2000 K) are larger than those calculated using the Wiedemann-Franz law, due to the contribution of the thermal vibration of atoms to the thermal conductivity of Fe-Ni alloys. The empirical Wiedemann-Franz law relates thermal conductivity and electrical resistivity as follows

$$L_0 \times T = k \times \rho \quad (2)$$

with *k* the thermal conductivity, *ρ* the electrical resistivity, *L*₀ the Sommerfeld value of the Lorenz number ($2.445 \times 10^{-8} \text{ W} \Omega \text{ K}^{-2}$), and *T* the temperature (Wiedemann and Franz 1853). In the study by Watanabe et al. (2019), the measured thermal conductivities *k* are on average about 29.5% higher than the ones computed using the Wiedemann-Franz law. This implies that (1) the empirical Wiedemann-Franz law provides lower bound estimates of *k* for Fe-Ni alloys, and (2) at first approximation, an upper bound of *k* can be calculated assuming a 30% increase in thermal conductivity values computed using Equation 2.

Upper and lower bounds of thermal conductivity *k* of Fe, Fe-5S, and Fe-Ni(-S) alloys were computed using the experimentally

determined electrical resistivity values at 4.5 and 8 GPa. These estimates are presented in Figure 7 for temperatures >1000 K. The computed values of *k* show that Fe-Ni and Fe-Ni-S samples present a narrow range of low thermal conductivity values at 4.5 and 8 GPa [between ~12 and 20 W/(m·K)], which is consistent with their high electrical resistivity. A small temperature dependence is observed, with *k* slightly increasing with increasing temperature. These computed *k* values are comparable to the ones for Fe-5S at 4.5 GPa and to Fe-15.6P obtained from electrical measurements at a slightly lower pressure (3.2 GPa; Yin et al. 2019), but are significantly lower than the ones obtained for pure iron and Fe-5S at 8 GPa (Fig. 7). This would be consistent with the hypothesis that the pressure dependence of both electrical resistivity and thermal conductivity of Fe and Fe-5S alloys is more important than the one of Fe-Ni(-S) alloys (and possibly, Fe-P alloys).

Application to the core of small terrestrial bodies

The pressure and temperature conditions considered in this study are directly relevant to the cores of the Moon and of Ganymede (Fig. 1). Although there is a large uncertainty on the composition of these terrestrial cores, it has been suggested that S might be present as a major alloying component (e.g., Breuer et al. 2015; Rückriemen et al. 2015). Assuming a Fe-S core chemistry, numerical studies have suggested that the thermal conductivity of the Lunar core ranges from about 15 to 65 W/(m·K) (Laneuville et al. 2014), and a comparable range of 20–60 W/(m·K) has been used to model the cooling of Ganymede's core (Rückriemen et al. 2015). These thermal conductivity values come from computations (de Koker et al. 2012), not from experiments conducted at relevant pressure, temperature, and chemistry conditions. As shown in Figure 7a, only the lower bound of these assumed *k* estimates overlaps with the thermal conductivity estimates of Fe-Ni(-S) alloys. This suggests that these core models may have assumed *k* values that are too high. It could be a significant issue because the thermal conductivity determines the heat flow down the adiabat, and thus, the presence and structure of any thermally stratified layer at the top of the core and the power available to generate a dynamo.

The adiabatic heat flux (*q*_a) can be estimated using the following equation

$$q_a = -k \times \frac{dT_a}{dr} \text{ with } \frac{dT_a}{dr} = -\alpha \times g \times \frac{T_a}{C_p} \quad (3)$$

with *k* the thermal conductivity, *dT*_a/*dr* the adiabatic temperature gradient across the core, and

$$-\alpha \times g \times \frac{T_a}{C_p}$$

being evaluated at radius *r*. The following values were considered: *C*_p = 830 J/kg/K, *g* = 1 m/s² (Ganymede) or 0.6 m/s² (Moon). Adiabatic temperatures *T*_a come from Breuer et al. (2015), who proposed two present-day adiabats for each of the two cores using the same values of *C*_p and *g* as above and a value of $\alpha = 9 \times 10^{-5} \text{ K}^{-1}$. *T*_a ranges from about 1280 to 1380 K or from 1640–1760 K for Ganymede's core and from about 1260 to 1600 K or from 1280–1630 K for the Lunar core, and the *T*_a profiles correspond to straight lines. It has been suggested that core chemistry can

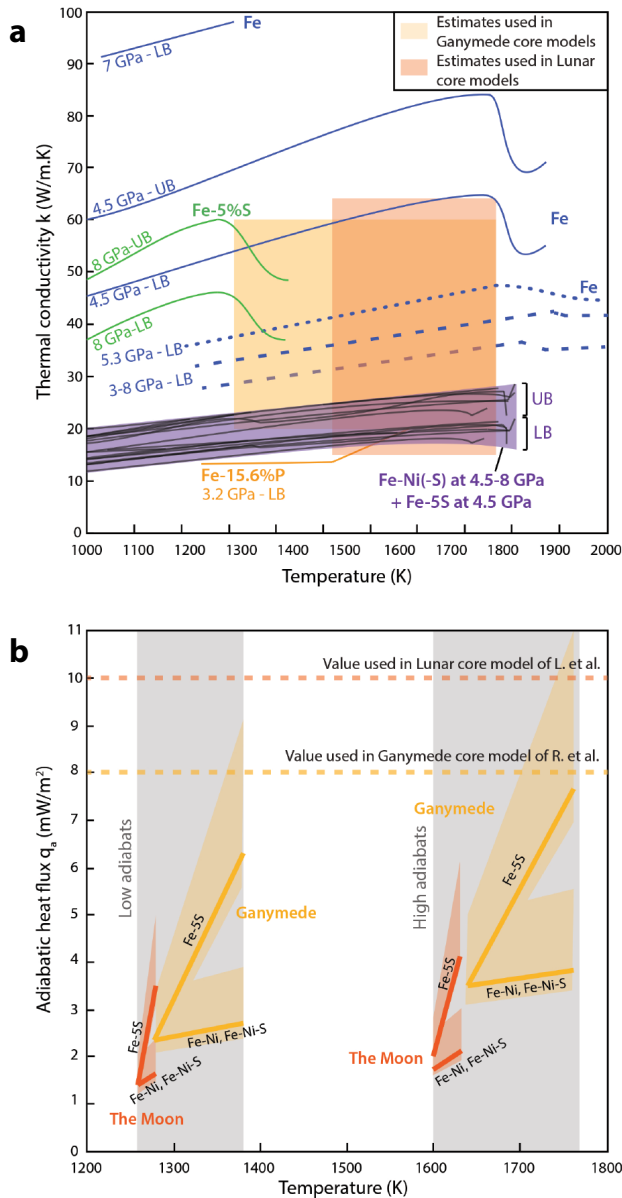


FIGURE 7. (a) Thermal conductivity (k) estimated from electrical measurements at 4.5 and 8 GPa as a function of temperature (LB = lower bound, UB = upper bound). All the estimates for Fe-Ni(-S) samples at 4.5 and 8 GPa and Fe-5S at 4.5 GPa fit into a narrow range of k values (gray lines in purple area). Comparison with estimates for Fe (blue) from Deng et al. (2013) (7 GPa), Secco and Schloessin 1989 (5.3 GPa) and Silber et al. (2018) (3–8 GPa), and for Fe-P from Yin et al. (2019) (3.2 GPa; orange line). Thermal conductivity decreases significantly when Ni is added to the core. The yellow and orange areas correspond to thermal conductivity estimates used as part of previous thermochemical models for the core of Ganymede (Rückriemen et al. 2015) and the Moon (Laneuville et al. 2013), respectively. (b) Adiabatic heat fluxes across Ganymede (yellow lines) and the Moon (red lines) cores, calculated using Equation 3 and α of thermal expansion value used in Breuer et al. (2015) ($9 \cdot 10^{-5} \text{ K}^{-1}$). The red and yellow shaded areas correspond to adiabatic heat fluxes obtained with a thermal expansion value of $1.05 \cdot 10^{-5}$ ($\pm 2.5 \cdot 10^{-5}$) K^{-1} (Williams 2009). Dashed lines correspond to the adiabatic heat flux values used in core modeling studies (Rückriemen et al. 2015 for Ganymede; Laneuville et al. 2013 for the Moon). The gray areas correspond to the low and high adiabats for both moons, from Breuer et al. (2015). See text for details. (Color online.)

affect modestly the slope of the adiabats (Williams 2009), but this steepening occurs at pressure higher than the core of the Moon or Ganymede. As mentioned in Williams (2009), there are two sets of values available for the thermal expansion of iron-rich nickel alloys coming from previous studies (Nasch and Manghnani 1998; Seifter et al. 1998), corresponding to 8×10^{-5} and $1.3 \times 10^{-4} \text{ K}^{-1}$, or 1.05×10^{-4} ($\pm 2.5 \times 10^{-5}$) K^{-1} , for the compositions considered in the present study. Calculations of q_a have therefore considered three different values of α (8×10^{-5} , 9×10^{-5} , and $1.3 \times 10^{-4} \text{ K}^{-1}$). The radius r of Ganymede's core is considered to be ~ 840 km and the one of the Lunar core to be ~ 330 km. In the case of a homogenous Fe-Ni(-S) core, assuming a constant k value across the core [taken to be 17 or 20 W/(m·K), for the lower and higher estimates of the adiabats, respectively] leads to q_a values of 2.36 or 3.82 mW/m² for Ganymede and 1.39 or 2.12 mW/m² for the Moon, depending on the adiabat considered and considering $\alpha = 9 \times 10^{-5} \text{ K}^{-1}$. Considering another α value (8×10^{-5} or $1.3 \times 10^{-4} \text{ K}^{-1}$) can lead to significant differences in heat flux estimates (colored shaded areas in Fig. 7b), illustrating therefore that adiabatic heat flux estimates are only as good as the experimental constraints on each parameter. The thermal conductivity of Fe-Ni(-S) being almost constant over the considered pressure range (Fig. 7a), calculating q_a using $k(r)$ (instead of a constant k value) results in very small ranges, as illustrated in Figure 7b: 2.36–2.69 or 3.47–3.82 mW/m² from across Ganymede's core and 1.39–1.67 or 1.77–2.12 mW/m² across the Lunar core, depending on the adiabat and considering the parameter values used in Breuer et al. (2015). In the case of a homogenous Ni-free, Fe-S core, the important pressure-dependence of k (Fig. 7a) leads to the following q_a ranges across the core: 2.36–6.28 or 3.47–7.63 mW/m² from across Ganymede's core and 1.39–3.50 or 2.03–4.24 mW/m² across the lunar core, depending on the adiabat (Fig. 7b). These q_a values correspond to an increase with depth by a factor of about 2–2.7 across the core. This factor could be higher than 2–2.7 in terrestrial bodies that have metallic cores spanning higher depth ranges than Ganymede and the Moon. In comparison, higher constant q_a values than the ones listed above were considered by Rückriemen et al. (2015) and Laneuville et al. (2014) (8 and 10 mW/m² for Ganymede and the Moon, respectively; Fig. 7b) and low q_a values (< 4 mW/m²) were considered in earlier core models (e.g., Hauck et al. 2006; Kimura et al. 2009). These q_a calculations have two major implications: (1) At first approximation, a constant k value can be assumed as part of Ni-bearing core models, whereas modeling Fe or Fe-S cores requires accounting for $k(r)$. (2) A similar amount of heat is conducted at any depth along the adiabat gradient of a Fe-Ni(-S) core, whereas less heat is conducted down this gradient at shallow depth in a Ni-free core. Because variation in heat conduction is critical to drive convection, this implies that it is possibly easier to drive convection in a Ni-free core than in a Ni-bearing core.

Another parameter to account for as part of k and q_a calculations across a metallic core is the possible heterogeneity of core composition as a function of depth that results from core cooling processes. Core fractional crystallization, which is expected in top-down or bottom-up cooling regimes, likely results in the heterogeneous distribution of light elements (such as S) across the core, characterized by the enrichment in light elements in the outer portion of the core (e.g., Breuer et al. 2015; Dumberry and

Rivoldini 2015; Rückriemen et al. 2015; Davies and Pommier 2018; Pommier 2018). New modeling studies considering the distribution and amount of nickel and light elements across the core are required to assess the importance of thermal conductivity gradients with depth on core convection.

ACKNOWLEDGMENTS

Part of this work was performed while the author was invited professor at the Université de Lille, France. The author is grateful to Anne-Marie Blanchemet for her help with SEM analyses and Séverine Bellanger for microprobe analyses at the electron probe microanalyzer (EPMA) facility in Lille. Both are part of the ARCHI-CM project, supported by the Ministère de l'Enseignement Supérieur et de la Recherche, Région Nord-Pas de Calais and European Regional Development Fund (ERDF). A.P. also thanks Sébastien Merkel for hosting her during her stay in Lille, and Christopher Davies and James Badro for fruitful discussions. The author is grateful to Heather Watson for her conscientious editorial work and two Reviewers for their thorough comments that improved the manuscript.

FUNDING

This work was supported by NSF-CAREER grant 1750746 and NSF-NERC grant 1832462. Use of the COMPRES Cell Assembly Project was supported by COMPRES under NSF Cooperative Agreement EAR 1661511. The electrical cell used in these experiments is available via COMPRES.

REFERENCES CITED

Argyriades, D., Derge, G., and Pound, G.M. (1959) Electrical conductivity of molten FeS. *Transactions of the Metallurgical Society of AIME*, 215, 909–912.

Anzellini, S., Dewaele, A., Mezouar, M., Loubeyre, P., and Morard, G. (2013) Melting of iron at Earth's inner core boundary based on fast X-ray diffraction. *Science*, 340, 464–466.

Breuer, D., Rückriemen, T., and Sphon, T. (2015) Iron snow, crystal floats, and inner-core growth: modes of core solidification and implications for dynamos in terrestrial planets and moons. *Progress in Earth and Planetary Sciences*, 2, 39. <https://doi.org/10.1186/s40645-015-0069-y>

Côté, A.S., Vocablo, L., and Brodholt, J.P. (2012) Ab initio simulations of iron–nickel alloys at Earth's core conditions. *Earth and Planetary Science Letters*, 345, 126–130.

Davies, C.J., and Pommier, A. (2018) Iron snow in the Martian core? *Earth and Planetary Science Letters*, 481, 189–200.

de Koker, N., Steinle-Neumann, G., and Vlcek, V. (2012) Electrical resistivity and thermal conductivity of liquid Fe alloys at high P and T , and heat flux in Earth's core. *Proceedings of the National Academy of Sciences*, 109 (11), 4070–4073.

Deng, L., Seagle, C., Fei, Y., and Shahar, A. (2013) High pressure and temperature electrical resistivity of iron and implications for planetary cores. *Geophysical Research Letters*, 40, 33–37.

Dumberry, M., and Rivoldini, A. (2015) Mercury's inner core size and core-crystallization regime. *Icarus*, 248, 254–268.

Elardo, S.M., and Shahar, A. (2017) Non-chondritic iron isotope ratios in planetary mantles as a result of core formation. *Nature Geoscience*, 10, 317–321.

Fei, Y., Li, J., Bertka, C.M., and Prewitt, C.T. (2000) Structure type and bulk modulus of Fe_3S , a new iron-sulfur compound. *American Mineralogist*, 85, 1830–1833.

Gomi, H., and Hirose, K. (2015) Electrical resistivity and thermal conductivity of hcp Fe–Ni alloys under high pressure: implications for thermal convection in the Earth's core. *Physics of the Earth and Planetary Interiors*, 247, 2–10.

Gomi, H., Ohta, K., Hirose, K., Labrosse, S., Caracas, R., Verstraete, M.J., and Hernlund, J.W. (2013) The high conductivity of iron and thermal evolution of the Earth's core. *Physics of the Earth and Planetary Interiors*, 224, 88–103.

Hansen, M. (1958) Constitution of Binary Alloys. McGraw-Hill, New York.

Hauck, S.A., Aurnou, J.M., and Dombard, A.J. (2006) Sulfur's impact on core evolution and magnetic field generation on Ganymede. *Journal of Geophysical Research*, 111, E09008. <https://doi.org/10.1029/2005JE002557>

Hayashi, H., Ohtani, E., Terasaki, H., and Ito, Y. (2009) The partitioning of Pt–Re–Os between solid and liquid metal in the Fe–Ni–S system at high pressure: Implications for inner core fractionation. *Geochimica et Cosmochimica Acta*, 73, 4836–4842.

Ho, C.Y., Ackerman, M., Wu, K., Havill, T., Bogaard, R., Matula, R., Oh, S., and James, H. (1983) Electrical resistivity of ten selected binary alloy systems. *Journal of Physics and Chemistry Ref. Data*, 12, 183–322.

Huang, D., and Badro, J. (2017) Fe–Ni ideality during core formation on Earth. *American Mineralogist*, 103, 1707–1710.

Huang, E., Bassett, W.A., and Weathers, M.S. (1988) Phase relationships in Fe–Ni alloys at high pressures and temperatures. *Journal of Geophysical Research*, 93, B, 7, 7741–7746.

Jarosewich, E. (1990) Chemical analyses of meteorites: a compilation of stony and iron meteorite analyses. *Meteoritics*, 25, 323–337.

Kantor, A., Kantor, I.Y., Kurnosov, A.V., Kuznetsov, A.Y., Dubrovinskaia, N.A., Krisch, M., Bossak, A.A., Dmitriev, V.P., Urusov, V.S., and Dubrovinsky, L.S. (2007) Sound wave velocities of fcc Fe–Ni alloy at high pressure and temperature by mean of inelastic X-ray scattering. *Physics of the Earth and Planetary Interiors*, 164, 83–89.

Kawaguchi, S.I., Nakajima, Y., Hirose, K., Komabayashi, T., Ozawa, H., Tateno, S., Kuwayama, Y., Tsutsui, S., and Baron, A.Q.R. (2017) Sound velocity of liquid Fe–Ni–S at high pressure. *Journal of Geophysical Research*, 122, 3624–3634. doi:10.1002/2016JB013609.

Kimura, J., Nakagawa, T., and Kurita, K. (2009) Size and compositional constraints of Ganymede's metallic core for driving an active dynamo. *Icarus*, 202(1), 216–224.

Kita, Y., and Morita, Z.-I. (1984) The electrical resistivity of liquid Fe–Ni, Fe–Co and Ni–Co alloys. *Journal of Non-Crystalline Solids* 61&62, 1079–1084.

Komabayashi, T., Pesce, G., Sinnyo, R., Kawazoe, T., Breton, H., Shimoyama, Y., Glazyrin, K., Konopková, Z., and Mezouar, M. (2019) Phase relations in the system Fe–Ni–Si to 200 GPa and 3900 K and implications for Earth's core. *Earth and Planetary Science Letters*, 512, 83–88.

Kuznetsov, A.Y., Dmitriev, V., Volkova, Y., Kurnosov, A., Dubrovinskaia, N., and Dubrovinsky, L. (2007) In-situ combined X-ray diffraction and electrical resistance measurements at high pressures and temperatures in diamond anvil cells. *High Pressure Research*, 27, 2, 213–222.

Laneuville, M., Wieczorek, M.A., Breuer, D., Aubert, J., Morard, G., and Rückriemen, T. (2014) A long-lived lunar dynamo powered by core crystallization. *Earth and Planetary Science Letters*, 401, 251–260. <https://doi.org/10.1016/j.epsl.2014.05.057>

Li, J., Fei, Y., Mao, H.K., Hirose, K., and Shieh, S.R. (2001) Sulfur in the Earth's inner core. *Earth and Planetary Science Letters*, 193, 509–514.

Lin, J.-F., Heinz, D.L., Campbell, A.J., Devine, J.M., Mao, W.L., and Shen, G. (2002) Iron–Nickel alloy in the Earth's core. *Geophysical Research Letters*, 29 (10), 1471. 10.1029/2002GL015089.

Lin, J.-F., Struzhkin, V.V., Sturhahn, W., Huang, E., Zhao, J., Hu, M.Y., Alp, E.E., Mao, H.-k., Boctor, N., and Hemley, R.J. (2003) Sound velocities of iron–nickel and iron–silicon alloys at high pressures. *Geophysical Research Letters* 30, 21, 2112. doi:10.1029/2003GL018405

Lin, J.-F., Fei, Y., Sturhahn, W., Zhao, J., Mao, H.-k., and Hemley, R.K. (2004) Magnetic transition and sound velocities of Fe_3S at high pressure: implications for Earth and planetary cores. *Earth and Planetary Science Letters* 226, 33–40.

lodders, K., and Fegley, B. Jr (1997) An oxygen isotope model for the composition of Mars. *Icarus*, 126, 373–394.

Ma, Y., Somayazulu, M., Shen, G., Mao, H.-K., Shu, J., and Hemley, R.J. (2004) In situ X-ray diffraction studies of iron to Earth-core conditions. *Physics of the Earth and Planetary Interiors*, 143–144, 455–467.

Mao, H.K., Wu, Y., Chen, L.C., Shu, J.F., and Jephcott, A.P. (1990) Static compression of iron to 300 GPa and $\text{Fe}_{0.8}\text{Ni}_{0.2}$ alloy to 260 GPa: implications for composition of the core. *Journal of Geophysical Research*, 95, 21737–21742.

Martorell, B., Brodholt, J., Wood, I.G., and Vocablo, L. (2013) The effect of nickel on the properties of iron at the conditions of Earth's inner core: ab initio calculations of seismic wave velocities of Fe–Ni alloys. *Earth and Planetary Science Letters*, 365, 143–151.

Martorell, B., Brodholt, J., Wood, I.G., and Vocablo, L. (2015) The elastic properties and stability of fcc-Fe and fcc-FeNi alloys at inner-core conditions. *Geophysical Journal International*, 202, 94–101.

McDonough, W.F., and Sun, S. (1995) The composition of the Earth. *Chemical Geology*, 120, 223–253.

Morard, G., Sanloup, C., Fiquet, G., Mezouar, M., Rey, N., Poloni, R., and Beck, P. (2007) Structure of eutectic Fe–FeS melts to pressures up to 17 GPa: Implications for planetary cores. *Earth and Planetary Science Letters*, 263, 128–139. doi:10.1016/j.epsl.2007.09.009.

Morrison, R.A., Jackson, J.M., Sturhahn, W., Zhao, J., and Toellner, T.S. (2019) High pressure thermoelasticity and sound velocities of Fe–Ni–Si alloys. *Physics of the Earth and Planetary Interiors*, 294, 106268. <https://doi.org/10.1016/j.pepi.2019.05.011>

Nasch, P.M., and Manghnani, M.H. (1998) Molar volume, thermal expansion, and bulk modulus in liquid Fe–Ni alloys at 1 bar: evidence for magnetic anomalies. In M.H. Manghnani and T. Yagi, Eds., *Properties of Earth and Planetary Materials at High Pressure and Temperature*. American Geophysical Union, Washington, D.C., pp. 307–317.

Pommier, A. (2018) Influence of sulfur on the electrical resistivity of a crystallizing core in small terrestrial bodies. *Earth and Planetary Science Letters*, 496, 37–46.

Pommier, A., Leinenweber, K., and Tran, T. (2019) Mercury's thermal evolution controlled by an insulating liquid outermost core? *Earth and Planetary Science Letters*, 517, 125–134.

Pozzo, M., and Alfè, D. (2016) Saturation of electrical resistivity of solid iron at Earth's core conditions. *SpringerPlus*, 5(1), p.256.

Righter, K., Go, B.M., Pando, K.A., Danielson, L., Ross, D.K., Rahman, Z., and Keller, L.P. (2017) Phase equilibria of a low S and C lunar core: Implications for an early lunar dynamo and physical state of the current core. *Earth and Planetary Science Letters*, 463, 323–332.

Rückriemen, T., Breuer, D., and Spohn, T. (2015) The Fe snow regime in Ganymede's core: a deep-seated dynamo below a stable snow zone. *Journal of Geophysical Research: Planets* 120, 1095–1118. <https://doi.org/10.1002/2014JE004781>

Sanloup, C., Guyot, F., Gillet, P., Fiquet, G., Mezouar, M., and Martinez, I. (2000) Density measurements of liquid Fe-S alloys at high-pressure. *Geophysical Research Letters*, 27 (6), 811–814.

Secco, R.A., and Schloessin, H.H. (1989) The electrical resistivity of solid and liquid Fe at pressures up to 7 GPa. *Journal of Geophysical Research*, 94 (B5), 5887–5894.

Seifert, A., Pottlacher, G., Jager, H., Groboth, G., and Kaschnitz, E. (1998) Measurements of thermophysical properties of solid and liquid Fe-Ni alloys. *Berichte der Bunsengesellschaft für physikalische Chemie*, 102, 1266–1271.

Silber, R.E., Secco, R.A., Yong, W., and Littleton, J.A.H. (2018) Electrical resistivity of liquid Fe to 12 GPa: Implications for heat flow in cores of terrestrial bodies. *Scientific Reports*, 8, 10758.

Stewart, A.J., Schmidt, M.W., van Westrenen, W., and Liebske, C. (2007) Mars: a new core-crystallization regime. *Science*, 316, 1323–1325.

Wagle, F., Steinle-Neumann, G., and de Koker, N. (2019) Resistivity saturation in liquid iron–light-element alloys at conditions of planetary cores from first principles computations. *Comptes Rendus Geoscience*, 351(2-3), 154–162.

Wakamatsu, T., Ohta, K., Yagi, T., Hirose, K., and Ohishi, Y. (2018) Measurements of sound velocity in iron–nickel alloys by femtosecond laser pulses in a diamond anvil cell. *Physics and Chemistry of Minerals*, 45, 589–595.

Wänke, H., and Dreibus, G. (1988) Chemical composition and accretion history of terrestrial planets. *Philosophical Transactions of the Royal Society of London*, 325, 545–557.

Watanabe, M., Adachi, M., and Fukuyama, H. (2016) Densities of Fe–Ni melts and thermodynamic correlations. *Journal of Materials Science*, 51 (7), 3303–3310.

Watanabe, M., Adachi, M., Uchikoshi, M., and Fukuyama, H. (2019) Thermal Conductivities of Fe-Ni melts measured by non-contact laser modulation calorimetry. *Metallurgical and Materials Transactions A*, 50, 3295–3300.

Wiedemann, D., and Franz, R. (1853) Über die Wärme-Leitfähigkeiten der Metalle. *Annals of Physics and Chemistry*, 89, 497–531.

Williams, Q. (2009) Bottom-up versus top-down solidification of the cores of small solar system bodies: Constraints on paradoxical cores. *Earth and Planetary Science Letters*, 284, 564–569.

Yin, Y., Zhai, K., Zhang, B., and Zhai, S. (2019) Electrical resistivity of iron phosphides at high-pressure and high-temperature conditions with implications for Lunar core's thermal conductivity. *Journal of Geophysical Research: Solid Earth*, 124, 5544–5556.

Zhang, L., and Fei, Y. (2008) Effect of Ni on Fe-FeS phase relations at high pressure and high temperature. *Earth and Planetary Science Letters*, 268, 212–218, doi:10.1016/j.epsl.2008.01.028.

MANUSCRIPT RECEIVED SEPTEMBER 25, 2019

MANUSCRIPT ACCEPTED JANUARY 29, 2020

MANUSCRIPT HANDLED BY HEATHER WATSON

Endnote:

¹Deposit item AM-20-77301, Supplemental Figure. Deposit items are free to all readers and found on the MSA website, via the specific issue's Table of Contents (go to http://www.minsocam.org/MSA/AmMin/TOC/2020/Jul2020_data/Jul2020_data.html).